

Simulation study of energetic-particle driven off-axis fishbone instabilities in tokamak plasmas

Hanzheng Li^{1,2}, Yasushi Todo^{1,2}, Hao Wang², Malik Idouakass²
and Jialei Wang²

¹ The University of Tokyo, Kashiwa, Chiba 277-8561, Japan

² National Institute for Fusion Science, National Institutes of Natural Sciences, Toki, Gifu 509-5292, Japan

E-mail: li.hanzheng@nifs.ac.jp

August 2021

Abstract. Kinetic-magnetohydrodynamic hybrid simulations were performed to investigate the linear growth and the nonlinear evolution of off-axis fishbone mode (OFM) destabilized by trapped energetic ions in tokamak plasmas. The spatial profile of OFM is mainly composed of $m/n = 2/1$ mode inside the $q = 2$ magnetic flux surface while the $m/n = 3/1$ mode is predominant outside the $q = 2$ surface, where m and n are the poloidal and toroidal mode numbers, respectively, and q is the safety factor. The spatial profile of the OFM is a strongly shearing shape on the poloidal plane, suggesting the nonperturbative effect of the interaction with energetic ions. The frequency of the OFM in the linear growth phase is in good agreement with the precession drift frequency of trapped energetic ions, and the frequency chirps down in the nonlinear phase. Two types of resonance conditions between trapped energetic ions and OFM are found. For the first type of resonance, the precession drift frequency matches the OFM frequency, while for the second type, the sum of the precession drift frequency and the bounce frequency matches the OFM frequency. The first type of resonance is the primary resonance for the destabilization of OFM. The resonance frequency which is defined based on precession drift frequency and bounce frequency of the nonlinear orbit for each resonant particle is analyzed to understand the frequency chirping. The resonance frequency of the particles that transfer energy to the OFM chirps down, which may result in the chirping down of the OFM frequency. A detailed analysis of the energetic ion distribution function in phase space shows that the gradient of the distribution function along the $E' = \text{const.}$ line drives or stabilizes the instability, where E' is a combination of energy and toroidal canonical momentum and conserved during the wave-particle interaction. The distribution function is flattened along the $E' = \text{const.}$ line in the nonlinear phase leading to the saturation of the instability.

1. introduction

Energetic particle confinement is an important issue of fusion research since energetic particles heat the fuel plasma to achieve the high temperature required for the fusion reaction. Magnetohydrodynamic (MHD) instabilities driven by energetic particles

such as fusion-born alpha particles and fast ions generated by neutral beam injection (NBI) and ion-cyclotron-range-of-frequency (ICRF) wave heating degrade the energetic-particle confinement. The interactions between energetic particles and MHD modes have been studied extensively over the decades [1, 2, 3, 4, 5, 6, 7, 8].

The classical fishbone mode located inside the $q = 1$ magnetic surface is a well-known MHD instability caused by the resonant interaction of energetic particles with MHD perturbations, where q is safety factor. The fishbone instability was first discovered in the Poloidal Divertor Experiment (PDX) with the nearly perpendicular NBI [9]. The fishbone instabilities were observed in periodic bursts with an $m/n = 1/1$ internal kink mode structure in the plasma, where m and n are poloidal and toroidal mode numbers, respectively. In the time evolution of the fishbone instabilities, the mode frequency is close to the precession drift frequency of deeply-trapped energetic particles at the beginning of the instability and chirps down significantly in the nonlinear phase associated with energetic particle losses. Since then, a considerable amount of work has been conducted theoretically and experimentally. The resonance between energetic particles and fishbones can be classified as follows:

- 1) Resonance with precession drift motion of trapped energetic particles. The fishbone mode is a kind of energetic particle mode (EPM).[10, 11]
- 2) The fishbone mode is an intrinsic kink mode with an oscillation of the order of the ion diamagnetic frequency.[12]
- 3) Resonance with the bounce motion of trapped energetic particles.[13]
- 4) Resonance with the circulating motion of passing energetic particles in the toroidal direction.[14, 15, 16]

A new energetic-particle driven MHD instability, off-axis fishbone mode (OFM), has been observed in JET, JT-60U, and DIII-D[17, 18, 19]. OFMs in plasmas with $q_0 \geq 1.5$ have been studied in JT-60U[20, 21, 22, 23] and DIII-D[23, 24, 22] tokamaks with higher β_N than that of JET. The frequency of OFM is close to the precession drift frequency of trapped energetic particles, which is similar to the classical fishbone. The OFM is supposed to transport the energetic particles away from the center as a trigger of the resistive wall mode (RWM) and the edge localized mode (ELM), preventing the high- β_N discharge. For the RWM, the impact of energetic-particle losses and rotation drop induced by the OFM is sufficient to destabilize the RWM since plasma rotation is the most efficient way to control the RWM [23]. In addition, a theoretical work[25] reveals that a mode conversion can occur between the RWM and precessional OFM. For the ELM, energetic particles transported by the OFM to the edge region may enhance the pressure gradient leading to the destabilization [21, 22].

This paper aims to investigate numerically the linear properties and the nonlinear evolution of OFM using kinetic-MHD hybrid simulation code MEGA, where plasma is described as an MHD fluid interacting with energetic particles. We constructed MHD equilibria via the Grad-Shafranov equation taking account of a DIII-D experiment [23]. It is found that the spatial profile of OFM is composed of $m/n = 2/1$ mode predominant

inside the $q = 2$ magnetic surface and $m/n = 3/1$ mode predominant outside the $q = 2$ surface. Parameter scans are performed on energetic-particle pressure, initial velocity distribution of energetic particles, and the location of the $q = 2$ surface for the linear frequency and the growth rate of OFM. The resonance condition analysis reveals that the contribution from the precession drift resonance is dominant, while another resonance through a combination of precession drift and bounce motion of trapped energetic particles yields a substantial contribution. The energetic-particle distribution function is analyzed carefully in phase space. All of the resonant energetic particles are concentrated around the $q = 2$ magnetic surface in the linear growth phase of the OFM, and they are transported radially in the nonlinear phase. The remainder of this paper is organized as follows. In Section 2, the physics model of the simulation is described. In Section 3, the simulation results are presented focusing on the linear properties of OFM and the wave-particle interaction. The nonlinear evolution of the OFM is presented in Section 4. Section 5 is devoted to discussion and summary.

2. Physics model

A kinetic-MHD hybrid simulation code MEGA[26, 27, 28, 29, 30, 31] is used for the simulations of OFM in this paper. In the physics model of MEGA, bulk plasma is treated as one fluid given by the nonlinear MHD equations, and the drift kinetic equations with δf particle-in-cell method are adopted for the energetic particles. The MHD equations with energetic-particle effects are given by

$$\frac{\partial \rho}{\partial t} = -\nabla \cdot (\rho \mathbf{v}) + \nu_n \nabla^2 (\rho - \rho_{eq}) \quad (1)$$

$$\begin{aligned} \rho \frac{\partial \mathbf{v}}{\partial t} = & -\rho \boldsymbol{\omega} \times \mathbf{v} - \rho \nabla \left(\frac{v^2}{2} \right) - \nabla p + (\mathbf{j} - \mathbf{j}'_h) \times \mathbf{B} \\ & - \nabla \times (\nu \rho \boldsymbol{\omega}) + \frac{4}{3} (\nu \rho \nabla \cdot \mathbf{v}) \end{aligned} \quad (2)$$

$$\frac{\partial \mathbf{B}}{\partial t} = -\nabla \times \mathbf{E} \quad (3)$$

$$\begin{aligned} \frac{\partial p}{\partial t} = & -\nabla \cdot (p \mathbf{v}) - (\gamma - 1) p \nabla \cdot \mathbf{v} \\ & + (\gamma - 1) \left[\nu \rho \omega^2 + \frac{4}{3} \nu \rho (\nabla \cdot \mathbf{v})^2 + \eta \mathbf{j} \cdot (\mathbf{j} - \mathbf{j}_{eq}) \right] \\ & + \chi \Delta (p - p_{eq}) \end{aligned} \quad (4)$$

$$\mathbf{E} = -\mathbf{v} \times \mathbf{B} + \eta (\mathbf{j} - \mathbf{j}_{eq}) \quad (5)$$

$$\boldsymbol{\omega} = \nabla \times \mathbf{v} \quad (6)$$

$$\mathbf{j} = \frac{1}{\mu_0} \nabla \times \mathbf{B} \quad (7)$$

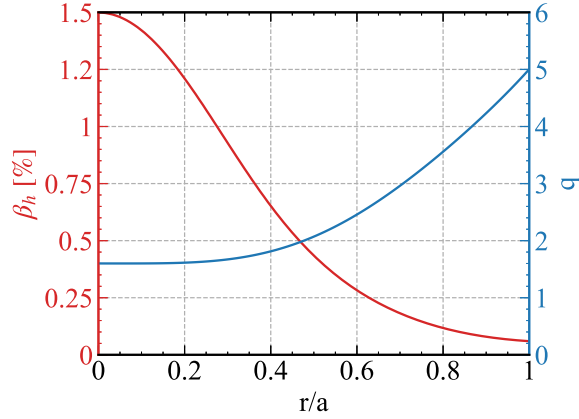


Figure 1: Spatial profiles of energetic-particle beta (red curve) and safety factor (blue curve).

where μ_0, γ are the vacuum magnetic permeability and adiabatic constant, respectively, the subscript ‘eq’ means the equilibrium, and ν and ν_n and χ are artificial viscosity and diffusion coefficients chosen to maintain numerical stability. Resistivity in Ohm’s law is represented by η . MEGA code solves these equations with a fourth-order finite difference scheme for spatial derivatives and the fourth-order Runge-Kutta method for time integration.

The energetic particle current density without $\mathbf{E} \times \mathbf{B}$ drift in Eq. (2) is given by

$$\mathbf{j}'_h = \int (\mathbf{v}_{\parallel}^* + \mathbf{v}_B) Z_h e f d^3v - \nabla \times \int \mu \mathbf{b} f d^3v \quad (8)$$

where $\mathbf{E} \times \mathbf{B}$ drift is not considered due to the quasi-neutrality[26], \mathbf{v}_{\parallel}^* includes the velocity parallel to the magnetic field and the velocity of magnetic curvature drift motion, \mathbf{v}_B is the velocity of magnetic gradient drift motion, and $Z_h e$, f , and μ are charge, distribution function, and magnetic moment for energetic particle, respectively. The second term on the right-hand side is the magnetization current.

Unless otherwise specified, the parameter in this paper is given as follows. We use the whole tokamak plasma domain with the toroidal angle range $0 \leq \phi < 2\pi$. Then, the simulation region is $R_c - a \leq R \leq R_c + a$, $0 \leq \phi < 2\pi$ and $-1.7a \leq Z \leq 1.7a$, where $R_c = 1.7$ m and $a = 0.6$ m are the major radius and the minor radius, respectively. The number of grid points is $128 \times 64 \times 128$ for cylindrical coordinates (R, ϕ, Z) with approximately 8×10^6 particles. The values of viscosity and diffusivity are set to be $\nu = 10^{-6} v_A R_c$ and $\nu_n = \chi = 0$, and the resistivity is $\eta = 10^{-7} \mu_0 v_A R_c$ in the simulations, where v_A is the Alfvén velocity at the plasma center. An anisotropic slowing-down distribution is used here to be consistent with the distribution of energetic particles in the experiments. The distribution function is given by

$$f_{eq}(\bar{\psi}, v, \Lambda) = C \exp\left(-\frac{\bar{\psi}}{\Delta\bar{\psi}}\right) \frac{1}{v^3 + v_{crit}^3} \times \frac{1}{2} \text{erfc}\left(\frac{v - v_{inj}}{\Delta v}\right)$$

$$\times \exp\left(-\frac{(\Lambda - \Lambda_0)^2}{\Delta\Lambda^2}\right) \quad (9)$$

where $\bar{\psi}$ is normalized poloidal magnetic flux with $\bar{\psi} = 0$ at the plasma center and $\bar{\psi} = 1$ at the plasma edge, and $\Delta\bar{\psi} = 0.3$. Pitch angle variable is represented by $\Lambda = \mu B_0/E$, where μ , B_0 , and E are magnetic moment, the magnetic field strength at the plasma center, kinetic energy of particles with Λ_0 and $\Delta\Lambda$ being the distribution peak location and width, respectively. In this paper, $\Lambda_0 = 1.1$ and $\Delta\Lambda = 0.1$ are used for all the cases. The background plasma is deuterium with the number density of $3 \times 10^{19} \text{ m}^{-3}$. The magnetic field strength at the plasma center is $B_0 = 1.7 \text{ T}$. The injection velocity of energetic particles is $v_{inj} = 0.58v_A$, corresponding to 80 keV deuterium neutral beam with $\Delta v = 0.1v_A$. The critical velocity is $v_{crit} = 0.62v_A$. The profiles of energetic-particle beta and safety factor are shown in Fig. 1. The energetic-particle beta profile is defined by

$$\beta_h(\bar{\psi}) = \beta_{h0} \exp(-\bar{\psi}/\Delta\bar{\psi}) \quad (10)$$

with β_{h0} the value at the center. A uniform bulk plasma beta profile with an initial value of 2.48% is assumed for simplicity. Regarding the safety factor, a parameter scan is carried out on safety factor profile, while the on-axis value and the edge value are kept the same as $q_{r=0} = 1.6$ and $q_{r=a} = 5.0$.

3. Simulation results

3.1. characteristics of OFM

Figure 2 shows the time evolution of the MHD perturbation energy (W) with $n = 1$ and the frequency of radial MHD velocity with $m/n = 2/1$, and the MHD pressure fluctuation profiles for different times in the standard run with $\beta_{h0} = 1.5 \times 10^{-2}$. We see the exponential growth and the saturation of the MHD perturbation energy at $t\omega_A \simeq 5177$ with $\omega_A = v_A/R_c$. The frequency of radial MHD velocity is $f_0 \simeq 12.3 \text{ kHz}$ before the saturation and chirps down along with the mode damping. The snapshots of the spatial structure of the MHD pressure fluctuations are shown for the linear and the nonlinear phases in Fig. 2(b) and (c). The linear phase shown in Fig. 2(b-i) exhibits that the mode is dominantly composed of the $m = 2$ harmonic inside the $q = 2$ magnetic surface drawn in solid line, while $m = 3$ is dominant outside the $q = 2$ surface. In particular, we see the strongly shearing profile of the OFM on the poloidal plane. The possible mechanism of the shearing structure of the OFM is the nonperturbative kinetic effects of energetic particles [32, 33, 34, 35, 36], as no shearing structure is observed in resistive kink mode. We see the shearing structure in the radial variation of the ratio of the $m = 2$ harmonic sine part to the cosine part shown in Fig. 2(c-i). The phase of the harmonics is chosen so that the cosine part of the dominant harmonic ($m = 2$) is maximized at the mode peak location. On the other hand, such a strongly shearing structure is not observed in the simulations of classical fishbone [29, 37]. During the damping phase, the $m = 2$ fluctuation profile becomes narrower in the radial direction,

while the $m = 3$ fluctuation is disappearing as shown in Fig. 2(b-iii). At the end of the simulation shown in Fig. 2(b-iv) and (c-ii), we can observe that the $m = 2$ harmonic profile is narrow with an outward shift in the radial direction and the relative amplitude of the sine part to the cosine part is enhanced. This indicates that the shearing profile is enhanced during the nonlinear evolution.

For a better understanding of OFM, we have performed a systematic scan of the central energetic-particle beta value β_{h0} on the mode growth rate and the frequency as shown in Fig. 3(a). Without energetic particles ($\beta_{h0} = 0\%$), we see that a resistive kink mode with the same $m/n = 2/1$ mode is unstable. With increasing β_{h0} , the kink mode is stabilized by energetic particles, and the OFM becomes unstable. We notice the appearance of the OFM by the jump in the mode frequency from 0 kHz to ~ 12 kHz. With increasing β_{h0} , the growth rate of the OFM increases while the frequency is kept almost constant in the range of 12.3 ± 0.5 kHz. In the present simulations, however, beta-induced Alfvén eigenmode (BAE)[38] becomes dominant for $\beta_{h0} > 1.5\%$ and limits the range of β_{h0} for the parameter scan for OFM. It is concluded that the OFM exhibits a similar relationship of the $q = 1$ fishbone mode to the kink mode[39].

In the experiments [18, 23], the initial mode frequency of OFM is close to the precession drift frequency of trapped energetic particles. Figure 3(b) shows the growth rate and the frequency of the OFM as a function of the injection velocity of energetic particles. The mode frequency increases when the injection velocity increases from $0.47v_A$ to $0.66v_A$. Meanwhile, the growth rate of OFM decreases. The results indicate that the mode frequency depends on the orbit frequency of the energetic particle. In particular, the precession drift frequency of deeply trapped particles is approximately given by [40]

$$\omega_d = \frac{Eq}{m_h r R_c \Omega_0} \quad (11)$$

where E , m_h , and Ω_0 are kinetic energy, mass, and gyro frequency of the energetic particle, respectively. For the specific case of $v_{inj} = 0.58v_A$, the mode frequency is 12.3 kHz, which is consistent with the precession drift frequency 14.3 kHz for $v = v_{inj}$. This suggests that the trapped energetic particles drive the OFM. Further details are discussed in the next subsection.

In previous studies [41], the effects of the radial location of the $q = 1$ magnetic flux surface were investigated for the classical fishbone. We performed a series of simulations to investigate the effect of the $q = 2$ magnetic flux surface location on the OFM. The safety factor profiles we used are shown in Fig. 3(c). Figure 3(d) shows the growth rate and the frequency of the OFM versus the normalized radius of the $q = 2$ magnetic flux surface ($r_{q=2}$). We see in the figure that the growth rate is an increasing function of $r_{q=2}$, and the mode frequency has a slight reduction. It indicates that the OFM becomes more unstable with increasing radius of the $q = 2$ magnetic flux surface. This effect is similar to that of the radius of the $q = 1$ magnetic flux surface on the classical fishbone.

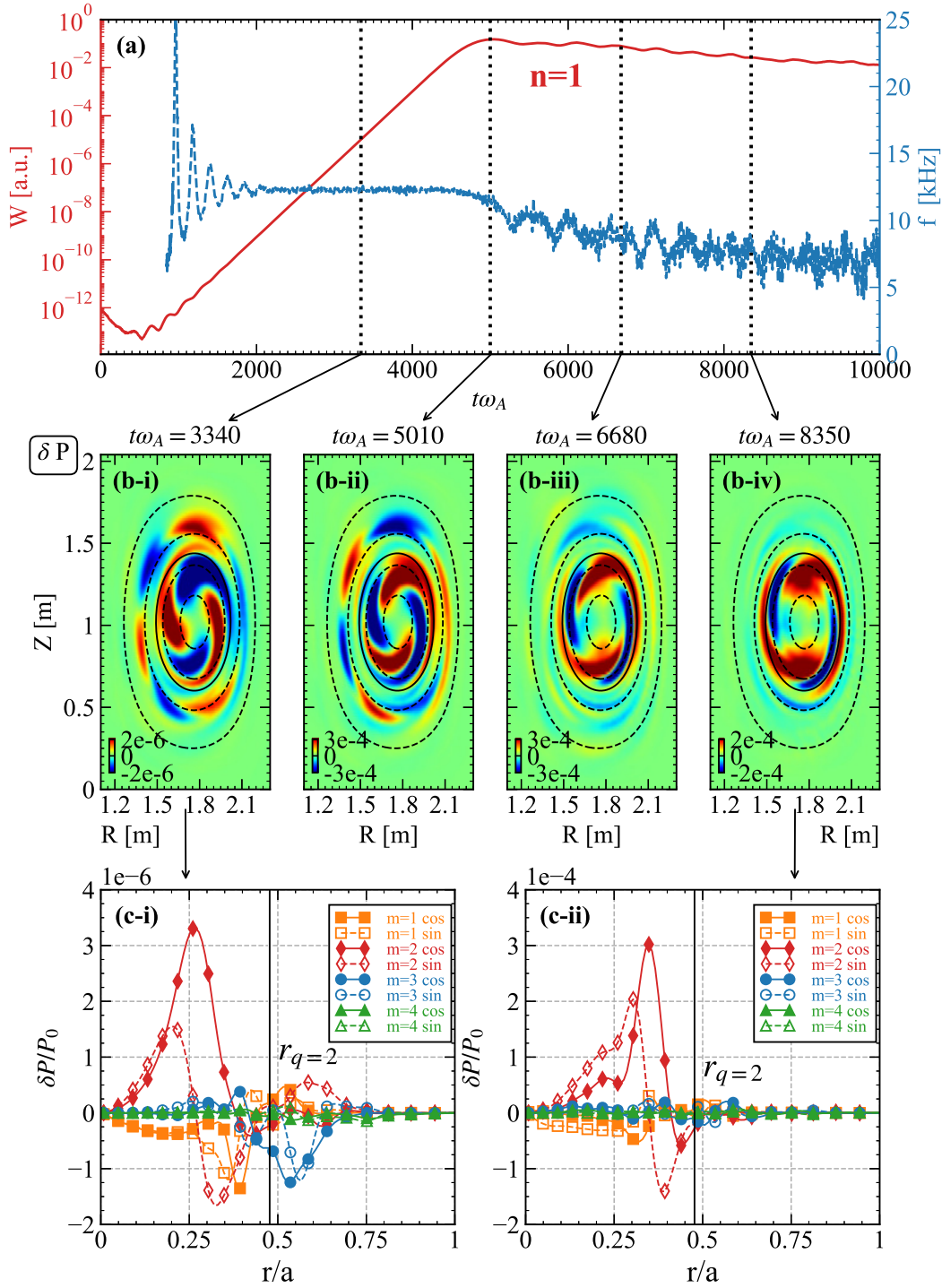


Figure 2: (a) Time evolution of MHD perturbation energy for $n = 1$ mode (red) and frequency of radial MHD velocity with $m/n = 2/1$ (blue). (b) Spatial structures of MHD pressure perturbation for different times. The $q = 2$ magnetic flux surface and other surfaces for $r/a = 0.2, 0.4, 0.6, 0.8$ are plotted with black solid and dashed lines, respectively. (c) Radial structures of MHD pressure perturbation at the linear growth phase and the nonlinear phase, respectively. Solid (dashed) lines with symbols represent the cosine (sine) parts of Fourier components. The location of the $q = 2$ magnetic flux surface is denoted by black solid lines.

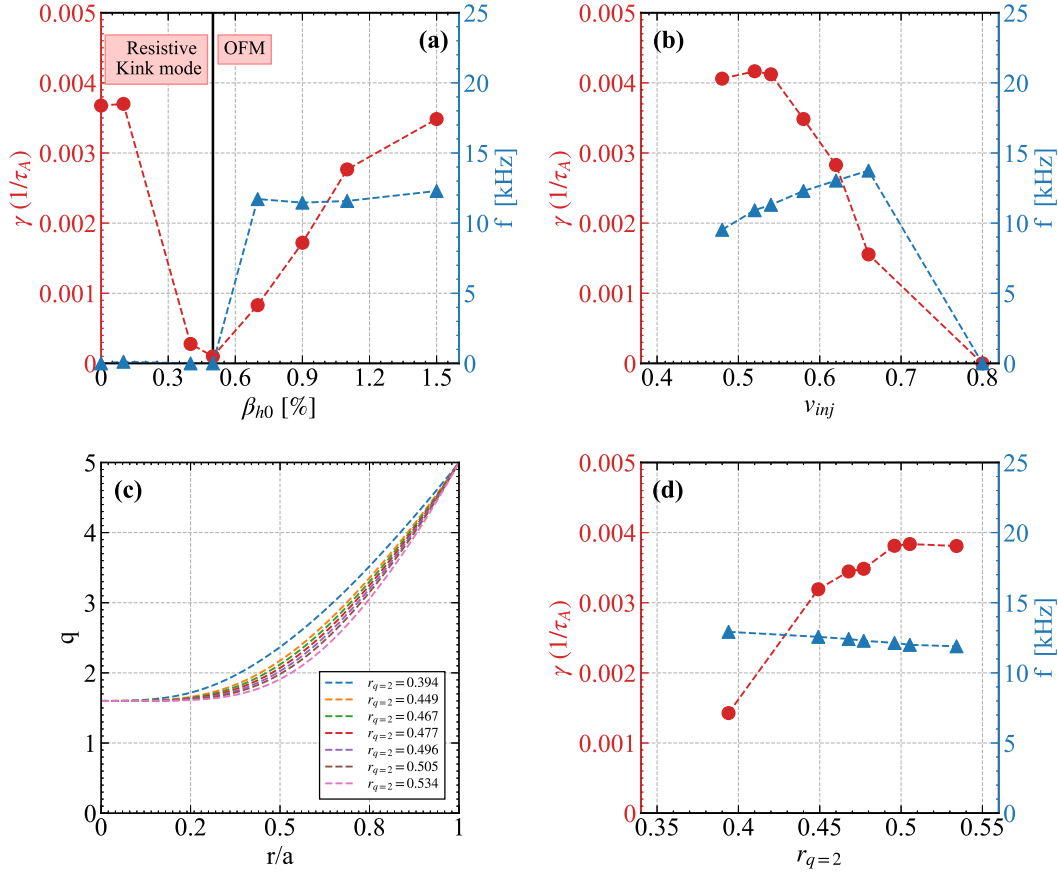


Figure 3: Linear growth rate (red circle) and mode frequency (blue triangle) versus (a) β_{h0} , (b) v_{inj} , and (d) normalized radius of the $q = 2$ magnetic flux surface ($r_{q=2}$). The data points shown in panel (d) are investigated by using the safety factor profiles shown in panel (c).

3.2. Resonance condition of energetic particles

We have picked up energetic particles with large $|\delta f|$ to clarify the resonance condition with the OFM. Particles with large $|\delta f|$ represent strong interaction with the OFM and can be regarded as resonant particles. The top 8000 energetic particles with large $|\delta f|$ are shown in (μ, Λ) space in Fig. 4(a). We classify the particles with large $|\delta f|$ into three types, Type I-III. Type I particles represented by black triangles in the figure are widely distributed in the range of $0.07 \leq \mu/(m_h v_A^2/B_0) \leq 0.19$ and $1.08 \leq \Lambda \leq 1.2$. Type II particles represented by blue circles are distributed around $\mu/(m_h v_A^2/B_0) = 0.02$ and $0.97 \leq \Lambda \leq 1.07$. Type III particles represented by red circles are distributed around $\mu/(m_h v_A^2/B_0) = 0.02$ and $1.1 \leq \Lambda \leq 1.2$.

Here, it should be noted that the OFM is the most unstable when the pitch angle variable is set to be $\Lambda_0 = 1.1$ among $\Lambda_0 = 1.0, 1.05, 1.1, 1.15, 1.2$ with $\Delta\Lambda = 0.1$ in the initial distribution function of energetic particles. The OFM is stable for $\Lambda_0 = 1.0$ and 1.2.

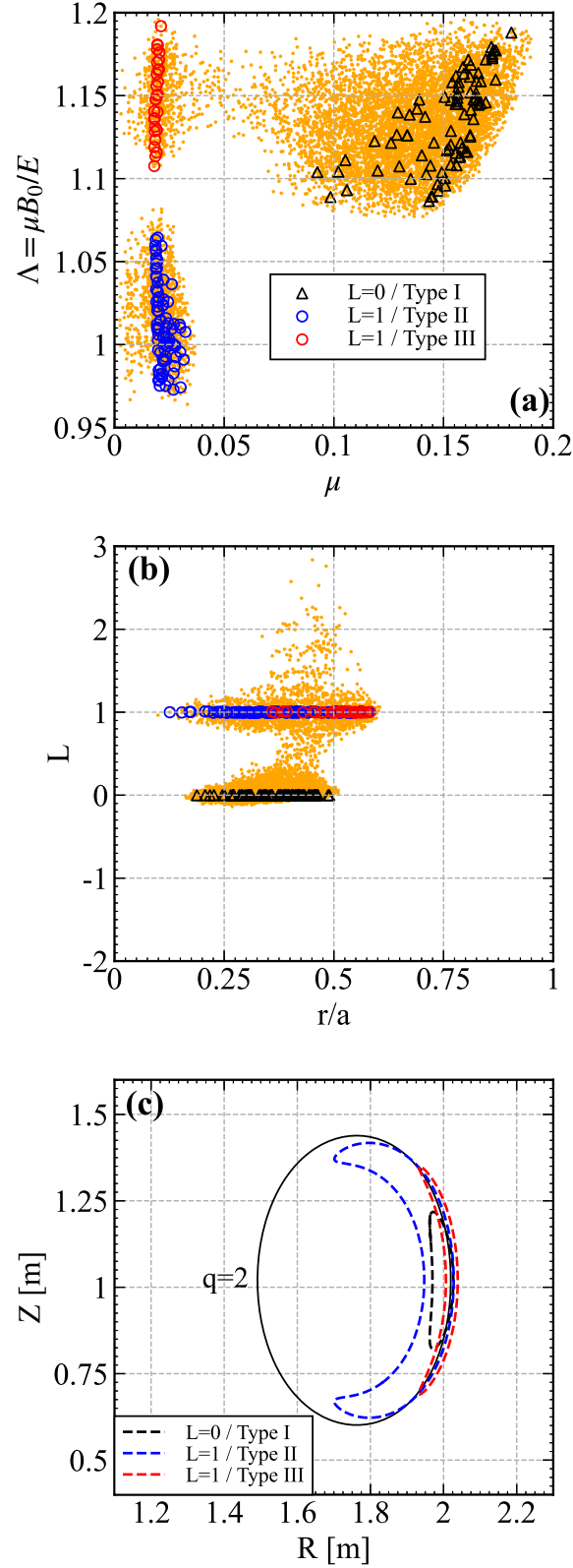


Figure 4: (a) Top 8000 energetic particles with large $|\delta f|$ in (μ, Λ) space, where μ is normalized by $m_h v_A^2 / B_0$. Black triangles, blue circles, and red circles represent Type I, Type II, and Type III particles, respectively. (b) Distribution of the top 8000 particles in $[r, (\omega_0 - n\omega_\phi)/\omega_\theta]$ space. (c) Typical orbits of the three types of resonant particles and the $q = 2$ magnetic flux surface.

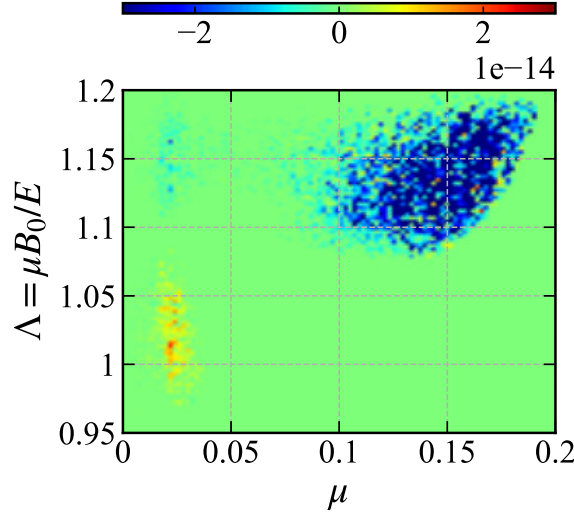


Figure 5: Distribution of energy transfer rate $w \frac{dE}{dt}$ in (μ, Λ) space, corresponding to Fig. 4(a). Blue color represents energy transfer from particles to the OFM, while red color represents energy transfer from the OFM to particles.

The resonance condition with a wave, of which frequency ω_0 is sufficiently lower than the cyclotron frequency in a tokamak, is [26, 42]

$$\omega_0 - L\omega_\theta - n\omega_\phi = 0 \quad (12)$$

where n is the toroidal mode number of the wave, and L is an integer representing the poloidal resonance number, ω_θ and ω_ϕ are poloidal and toroidal orbit frequency of the particle, respectively. For trapped particles, ω_θ is the bounce frequency and ω_ϕ is the precession drift frequency. We plot the values of $(\omega_0 - n\omega_\phi)/\omega_\theta$ for the top 8000 particles in Fig. 4(b). The horizontal axis of the figure is the normalized radial location of the particles. We see that the values are concentrated around 0 and 1, indicating that the resonance occurs with $L = 0$ for Type I particles and $L = 1$ for Type II and III particles. The typical orbits for the three types of particles are plotted in (R, Z) plane in Fig. 4(c). All of the orbits are located close to the $q = 2$ magnetic flux surface, which leads to the strong interaction with the OFM. This may also explain why the OFM is the most unstable for $\Lambda_0 = 1.1$. The pitch-angle variable for the Type I and Type III particles shown in Fig. 4(c) is $\Lambda = 1.15$. For $\Lambda_0 = 1.1$ and $\Lambda = 1.15$, the pitch-angle distribution $G = \exp\left(-\frac{(\Lambda - \Lambda_0)^2}{\Delta\Lambda^2}\right)$ given by Eq. (9) leads to the strong drive to the OFM through the energy derivative $\left.\frac{\partial G}{\partial E}\right|_{\mu=\text{constant}} = 2(\Lambda - \Lambda_0)(\mu B_0/E^2 \Delta\Lambda^2)G > 0$ [43].

The energy transfer rate $w \frac{dE}{dt}$ is analyzed for energetic particles in (μ, Λ) space, where w is the particle weight, dE/dt is the time derivative of kinetic energy of the particle. The result is shown in Fig. 5. The region with $w \frac{dE}{dt} < 0$ represented by blue color transfers energy to the OFM and drives the instability. We can see that Type I particles are the primary component for the destabilization of the OFM, while Type III particles also provide a weak contribution. In contrast, Type II particles obtain energy

stabilizing the OFM. The primary resonance between the OFM and energetic particles is the precession drift resonance with $L = 0$. This is consistent with the theoretical study which predicts that OFM with external kink mode profile can be excited when trapped energetic-particle beta exceeds a critical value [25]. The spatial profile of OFM in our simulation is different from the external kink mode profile which was assumed in the theory. In addition, we have found a new resonance with $L = 1$ for a relatively low magnetic moment with a similar Λ to the primary resonance. Since Λ is comparable between the two resonances, the low magnetic moment is equivalent to low energy. The new resonance with $L = 1$ occurs for Type II and III particles with relatively low energy. It is interesting to note that Type II particles with lower Λ obtain energy from the OFM while Type III particles with higher Λ give energy. This will be investigated in detail in the next section.

4. Nonlinear evolution

4.1. Evolution of particle orbit frequency

The nonlinear dynamics and transport of energetic particles are investigated in this section. We see in Fig. 2(a) that the OFM grows exponentially with the initial frequency $f_0 = 12.3$ kHz, and the frequency chirps down to around 7.4 kHz during the nonlinear phase. We define the resonance frequency $\omega_{resonant}$ by

$$\omega_{resonant} = n\omega_\phi + L\omega_\theta . \quad (13)$$

Here, we should emphasize that ω_ϕ and ω_θ are nonlinear orbit frequencies measured during the nonlinear simulation following the particle orbit interacting with the MHD perturbations. Distributions of the top 8000 energetic particles with large $|\delta f|$ are shown in $(\omega_\phi, \omega_{resonant})$ space for different times in Fig. 6. Red (blue) color represents positive (negative) δf in the figure. For the linear growth phase of the OFM shown in Fig. 6(a), we see that the resonance frequency for both $L = 0$ and $L = 1$ particles are almost the same as the mode frequency represented by the dashed line. The $L = 0$ and $L = 1$ particles are located around $\omega_\phi = 0.0285\omega_A$ and $\omega_\phi = 0.004\omega_A$, respectively. For $t\omega_A = 4008$ shown in Fig. 6(b), the resonance frequency begins to chirp down (up) for positive (negative) δf particles shown in red (blue). It indicates that a weak effect of nonlinearity exists before the saturation. For $t\omega_A = 5010$ at the saturation of the instability, we see in Fig. 6(c) a large down-shift in resonance frequency for positive δf particles and a significant up-shift for negative δf particles. At the same time, we see a slight decrease in the mode frequency in Fig. 2(a).

In the nonlinear phase shown in Fig. 6(d), the separation in resonance frequency between positive and negative δf particles develops further. The resonance frequency of the particles with positive δf decreases along with the chirping-down of the OFM frequency. These particles may be kept resonant with the OFM. This suggests a different mechanism of frequency chirping from recent studies of classical fishbone where the

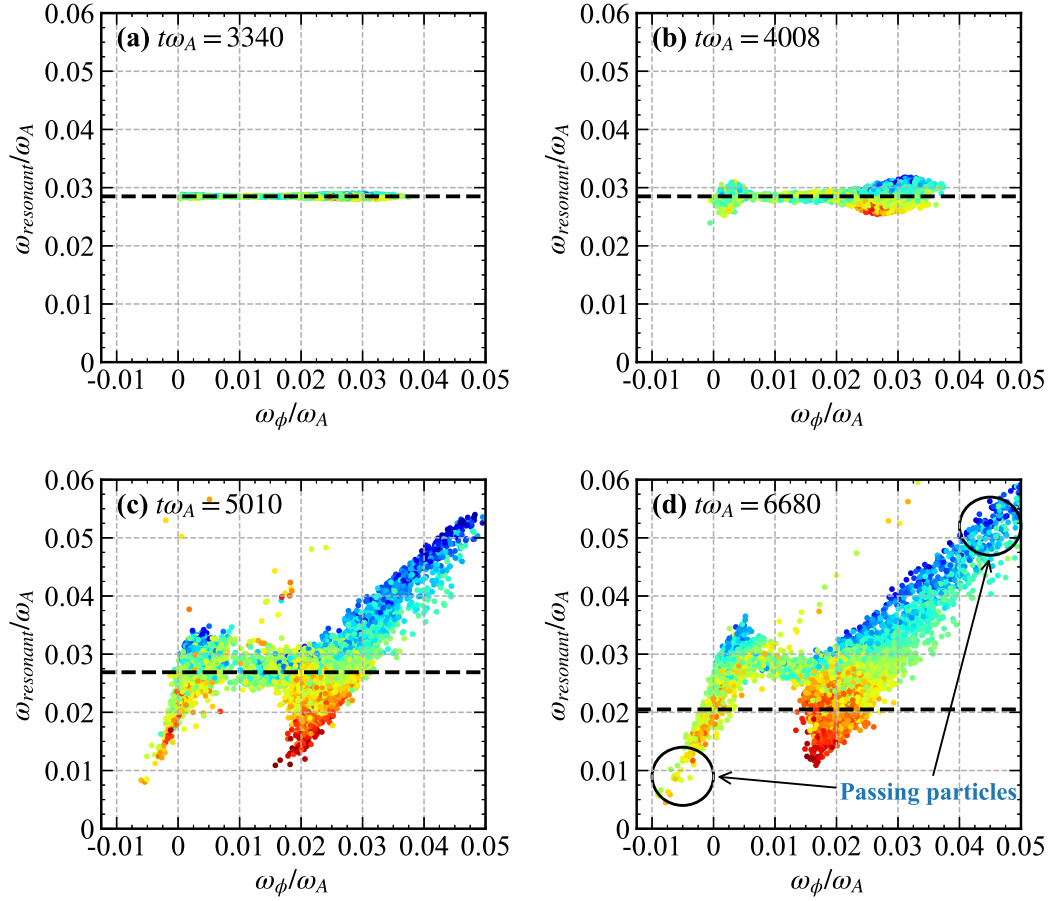


Figure 6: Distributions of the top 8000 energetic particles with large $|\delta f|$ in $(\omega_\phi, \omega_{\text{resonant}})$ space at (a) $t\omega_A = 3340$, (b) $t\omega_A = 4008$, (c) $t\omega_A = 5010$ and (d) $t\omega_A = 6680$. Red (blue) color represents positive (negative) δf . The mode frequency of the OFM at each time is represented by black dashed line. The $L = 0$ and $L = 1$ particles are located around $\omega_\phi = 0.0285\omega_A$ and $\omega_\phi = 0.004\omega_A$, respectively, in panel (b).

frequency down-chirping is attributed to the flattening of the energetic particle pressure profile [44].

In addition, the transition from trapped particle to passing particle is observed in the nonlinear phase. It should be noted that for some $L = 1$ particles, the precession drift frequency decreases to zero, and changes the sign. These particles become passing particles moving in $-\phi$ direction.

4.2. Distribution function analysis

We have analyzed the energetic-particle distribution function to understand the physical mechanisms of destabilization and stabilization in the linear growth and nonlinear phases. Figure 7 illustrates distribution function perturbations in (P_ϕ, E) space for

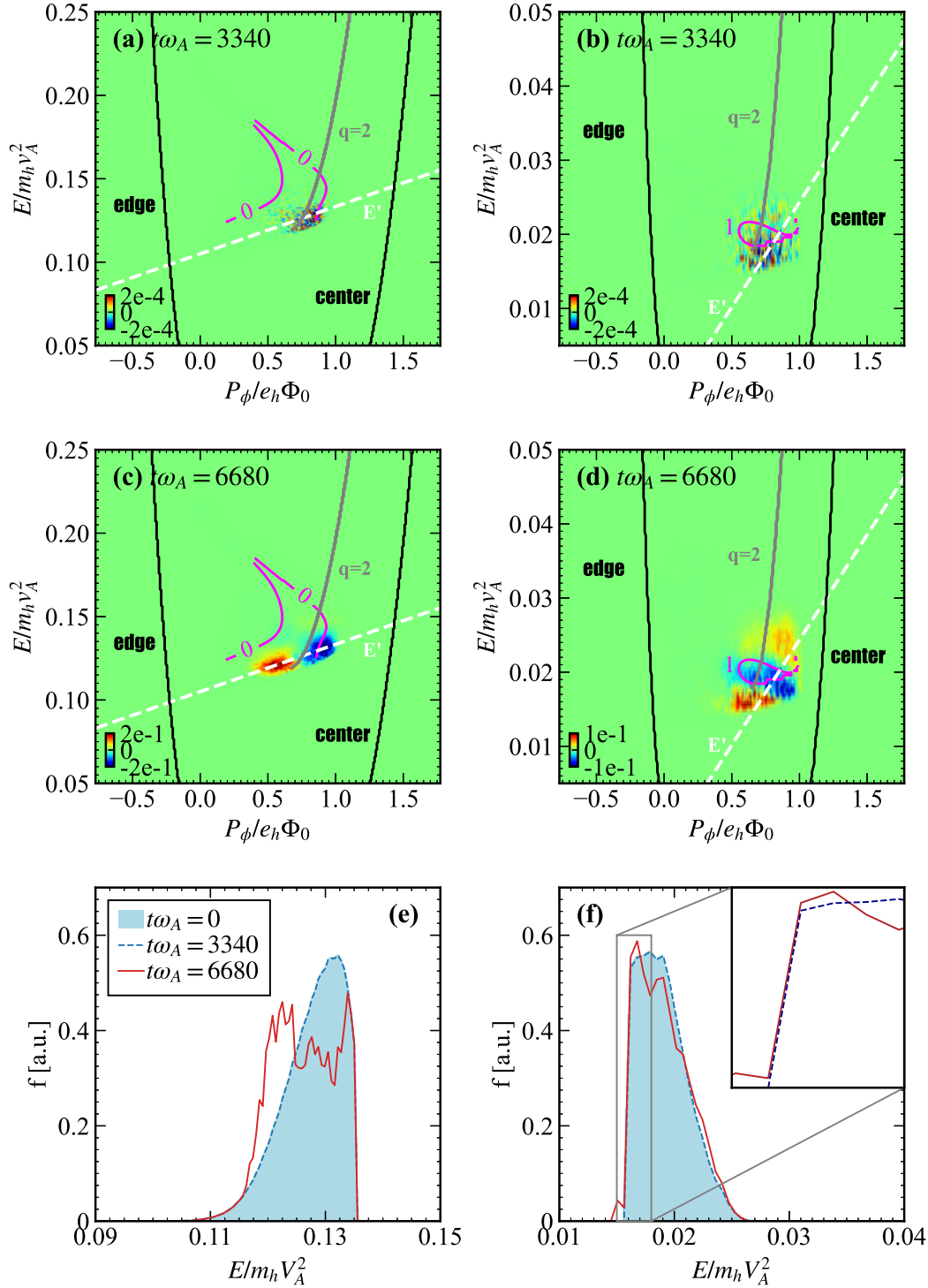


Figure 7: Energetic-particle distribution function perturbations in (P_ϕ, E) space with $\mu = 0.14$ ($L = 0$) and $\mu = 0.02$ ($L = 1$) are shown in left and right columns, respectively, for [(a) and (b)] $t\omega_A = 3340$ and [(c) and (d)] $t\omega_A = 6680$. Magenta lines represent resonance condition with the OFM, where resonance integer L is labeled. The white dashed lines represent $E' = \text{const.}$ The location of the $q = 2$ magnetic flux surface is denoted by gray lines. Energetic-particle distribution functions along the $E' = \text{const.}$ lines are compared between different times for (e) $\mu = 0.14$ and (f) $\mu = 0.02$.

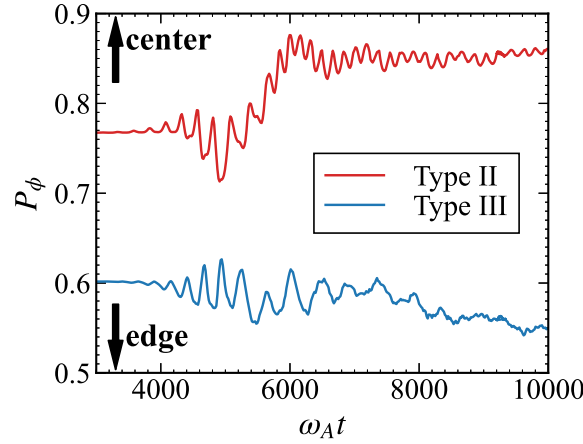


Figure 8: Time evolution of P_ϕ for Type II (red curve) and Type III (blue curve) particles with positive δf .

a particular value of $\mu = 0.14m_h v_A^2/B_0$ ($\mu = 0.02m_h v_A^2/B_0$) in top (middle) panels for different times. There are three variables, toroidal canonical momentum (P_ϕ), kinetic energy (E), and magnetic moment (μ) with the definition $P_\phi = e_h \Psi + m_h R v_\parallel b_\phi$, $E = \frac{1}{2} m_h v^2$, and $\mu = \frac{1}{2} m_h v_\perp^2/B$. For the interaction with Alfvén eigenmodes whose frequency is sufficiently lower than the ion Larmor frequency, magnetic moment μ is an adiabatic invariant. At the plasma core, the poloidal magnetic flux is set to Ψ_0 , and at the plasma border, it is set to 0. The energetic particle is denoted by the subscript “h” while the ϕ component of the magnetic field unit vector is denoted by b_ϕ . All the particles in the simulation are included for the integration of the δf distribution. The magenta lines are the contours of

$$F(\omega_\phi, \omega_\theta) = \frac{\omega - n\omega_\phi}{\omega_\theta} \quad (14)$$

where ω_ϕ and ω_θ are measured following particle orbits in the equilibrium magnetic field for the linear resonance condition [31]. The magenta lines represent the resonance condition $F(\omega_\phi, \omega_\theta) = L$ where L is an integer and labeled in the figure. In the linear growth phase shown in Fig. 7(a) and (b), resonance regions between the OFM and energetic particles emerge. It should be noted that the resonance regions are close to the $q = 2$ magnetic flux surface represented by gray lines in both figures. The total distribution function is almost the same as the initial distribution function as shown in Fig. 7(e) and (f). After the saturation, we see in Fig. 7(c) and (d) that positive (negative) δf regions shown in red (blue) appear along the $E' = E - \frac{\omega}{n} P_\phi = \text{const.}$ lines, which is conserved during the wave-particle interaction when the frequency chirping is neglected [8, 45]. It is found in Fig. 7(d) that for $L = 1$ particles, the two pairs of resonance regions are created while the blue regions overlap each other. These two pairs are Type II and III particles. Type II particles stabilize the OFM on the higher-energy side, while Type III particles are located on the lower-energy side. Figure 8 clearly

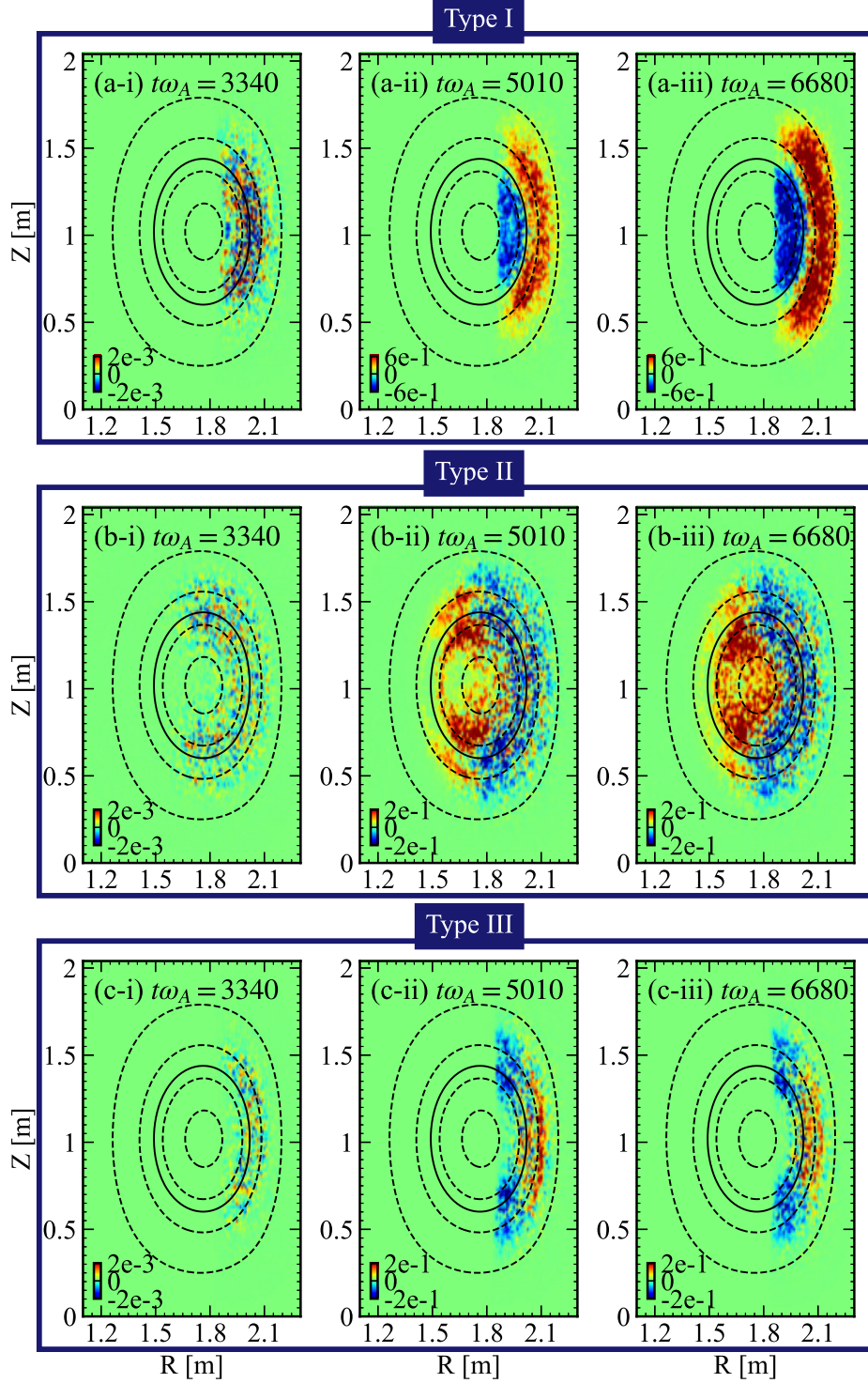


Figure 9: Series of poloidal snapshots for energetic particle distribution perturbations of the top 8000 particles with large $|\delta f|$ for (a) type I particles ($L = 0$), (b) type II particles ($L = 1$) and (c) type III particles ($L = 1$) at (a-i) (b-i) (c-i) $t\omega_A = 3340$, (a-ii) (b-ii) (c-ii) $t\omega_A = 5177$, (a-iii) (b-iii) (c-iii) $t\omega_A = 6680$. Red (blue) color represents positive (negative) δf . The $q = 2$ magnetic flux surface is represented by black solid lines and other magnetic flux surfaces are represented by dashed lines for $r/a = 0.2, 0.4, 0.6, 0.8$.

shows that the type II and type III particles with positive δf tend to move radially inward and outward, respectively. It means that Type II (III) particles move to the center (edge), matching the right (left) pair of the resonant regions shown in Fig. 7(d). The oscillation of typical particles shown in Fig. 8 suggests that they are trapped by the wave.

We see in Fig. 7(e) and (f) that the distribution function is flattened along the $E' = \text{const.}$ lines around the resonance due to (inverse) Landau damping significantly in Fig. 7(e) and moderately in Fig. 7(f). The energy derivative of the distribution function along an $E' = \text{const.}$ line is defined by [8, 31]

$$\left. \frac{\partial f}{\partial E} \right|_{E'} = \frac{\partial f}{\partial E} + \frac{dP_\phi}{dE} \frac{\partial f}{\partial P_\phi} = \frac{\partial f}{\partial E} + \frac{n}{\omega} \frac{\partial f}{\partial P_\phi} \quad (15)$$

where n and ω are toroidal mode number and mode frequency. The right-hand side of the equation represent the drive for the inverse Landau damping or the damping for Landau damping. We see in Fig. 7(e) and (f) that $df/dE > 0$ along the $E' = \text{const.}$ lines at $t\omega_A = 0$ causes the inverse Landau damping and drives the OFM for Type I particles with $L = 0$ and Type III particles with $L = 1$. The saturation of the instability can be attributed to the significant flattening of the distribution function along the $E' = \text{const.}$ lines as shown in Fig. 7(e). In Fig. 7(f), the negative gradient of distribution function causes the Landau damping to stabilize the OFM. This phase space region corresponds to Type II particles.

4.3. Distribution evolution in (R, Z) plane

Furthermore, the top 8000 resonant particles with large $|\delta f|$ are chosen to plot the energetic particle distribution perturbations in an (R, Z) plane. In the linear growth phase shown in Fig. 9(a-i), (b-i) and (c-i), the resonant interaction is taking place around the $q = 2$ magnetic flux surface. In the nonlinear phase, we see that the red regions ($\delta f > 0$) move radially outward and blue regions ($\delta f < 0$) move inward for Type I particles shown in Fig. 9(a-ii) and (a-iii), while the motion of Type II particles is in the opposite way as shown in Fig. 9(b-ii) and (b-iii). Type III particles move similarly to type I particles, although radial transport of positive and negative particles is weak, as seen in Fig. 9(c-ii) and (c-iii). In particular, we notice in Fig. 9(b-iii) that some Type II particles become passing particles near the plasma center due to the energy transfer from wave to particles. The perpendicular energetic-particle pressure profiles are compared for different times in Fig. 10. The initial profile is shown as a shaded region. The solid red line shows the flattening of the energetic-particle pressure profile at the end of the simulation and a substantial energetic-particle transport in the radial direction. Interestingly, the energetic-particle transport occurs not only at the saturation of the OFM ($t\omega_A = 5010$) but also during the frequency chirping after the saturation.

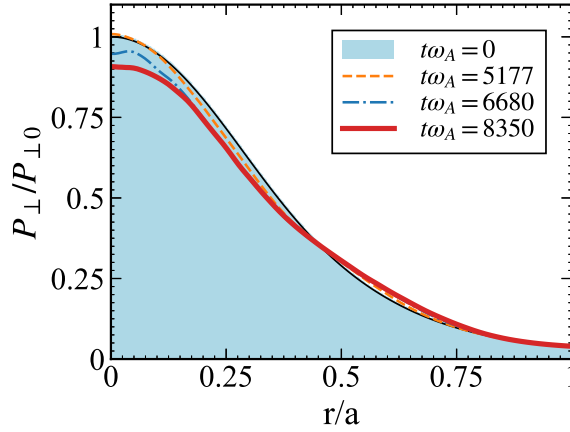


Figure 10: Perpendicular energetic-particle pressure profiles for different times. The OFM is saturated at $t\omega_A = 5010$.

5. Discussion and summary

We have investigated the linear growth and the nonlinear evolution of OFM destabilized by trapped energetic ions in tokamak plasmas with kinetic-MHD hybrid simulations. The spatial profile of the OFM is mainly composed of $m/n = 2/1$ mode inside the $q = 2$ magnetic flux surface while the $m/n = 3/1$ mode is predominant outside the $q = 2$ surface. The spatial profile of the OFM is a strongly shearing shape on the poloidal plane, suggesting the nonperturbative effect of the interaction with energetic ions. The frequency of the OFM in the linear growth phase is in good agreement with the precession drift frequency of trapped energetic ions, and the frequency chirps down in the nonlinear phase. The parametric scan showed that the OFM is significantly affected by energetic-particle pressure, injection velocity, and the radius of the $q = 2$ magnetic flux surface. It was found that two types of resonance with the poloidal resonance number $L = 0$ and $L = 1$ make a substantial contribution to the instability. The primary resonance between energetic particles and OFM is the precession drift resonance with $L = 0$. The resonance with $L = 1$ is a combination of precession drift and bounce motion and has both the destabilizing and the stabilizing effects on OFM. The contribution from the $L = 1$ resonance is weaker than that from the $L = 0$ resonance.

The resonance frequency, which is defined based on precession drift frequency and bounce frequency of the nonlinear orbit for each resonant particle, was analyzed to understand the frequency chirping. It was found that the resonance frequency of positive δf particles chirps down, which may result in the chirping down of the OFM frequency. We analyzed the energetic-ion distribution function in (P_ϕ, E) space. It was demonstrated that the gradient of the distribution function along the $E' = \text{const.}$ line drives or stabilizes the instability. The distribution function is flattened along the $E' = \text{const.}$ line in the nonlinear phase leading to the saturation of the instability. The energetic-ion pressure profiles for different times indicate that the energetic-ion

transport occurs not only at the saturation of the OFM but also during the frequency chirping after the saturation.

In the experiments, the magnetic probe signals in both JT-60U and DIII-D devices exhibit a strong waveform distortion (non-sinusoidal oscillation) synchronized with the energetic particle transport to the plasma edge [22, 23, 24]. The data from the toroidal array show that the mode distortion is related to the higher- n harmonics. This unique feature has never been reported for classical fishbone bursts. The higher- n harmonics are generated through MHD nonlinearity, which depends significantly on the mode amplitude and the spatial profile. The shearing profile of the OFM found in this work may affect the waveform distortion observed at a specific location through the spatial profile of the nonlinearly generated modes. The waveform distortion will be investigated in our future work, where the numerical resolution and the dissipations should be considered carefully.

Acknowledgments

Numerical computations were performed on the Plasma Simulator (NEC SX-Aurora TSUBASA) of NIFS with the support and under the auspices of the NIFS Collaboration Research program (NIFS20KNST169), the JFRS-1 of the International Fusion Energy Research Centre, and the Supercomputer Fugaku of the RIKEN Center for Computational Science (Project ID: hp210178). This work was supported by MEXT as Program for Promoting Researches on the Supercomputer Fugaku (JPMXP1020200103).

References

- [1] FASOLI, A., GORMENZANO, C., BERK, H., et al., Progress in the ITER Physics Basis Chapter 5: Physics of energetic ions 2007 Nucl. Fusion **47** S264.
- [2] HEIDBRINK, W. W., Physics of Plasmas **15** (2008) 055501.
- [3] BREIZMAN, B. N. and SHARAPOV, S. E., Plasma Physics and Controlled Fusion **53** (2011) 054001.
- [4] TOI, K., OGAWA, K., ISOBE, M., et al., Plasma Physics and Controlled Fusion **53** (2011) 024008.
- [5] SHARAPOV, S., ALPER, B., BERK, H., et al., Nuclear Fusion **53** (2013) 104022.
- [6] GORELENKOV, N. N., PINCHES, S. D., and TOI, K., Nuclear Fusion **54** (2014).
- [7] CHEN, L. and ZONCA, F., Rev. Mod. Phys. **88** (2016) 015008.
- [8] TODO, Y., Reviews of Modern Plasma Physics **3** (2018) 1.
- [9] MCGUIRE, K., GOLDSTON, R., BELL, M., et al., Phys. Rev. Lett. **50** (1983) 891.
- [10] CHEN, L., WHITE, R. B., and ROSENBLUTH, M. N., Phys. Rev. Lett. **52** (1984) 1122.
- [11] IDOUAKASS, M., *Linear and nonlinear study of the precessional fishbone instability*, PhD thesis, 2016, 2016AIXM4756.
- [12] COPPI, B. and PORCELLI, F., Phys. Rev. Lett. **57** (1986) 2272.
- [13] FREDRICKSON, E., CHEN, L., and WHITE, R., Nuclear Fusion **43** (2003) 1258.
- [14] BETTI, R. and FREIDBERG, J. P., Phys. Rev. Lett. **70** (1993) 3428.
- [15] WANG, S., Phys. Rev. Lett. **86** (2001) 5286.
- [16] YU, L., WANG, F., FU, G., and YU, L., Nuclear Fusion **59** (2019) 086016.
- [17] HUYSMANS, G., HENDER, T., ALPER, B., et al., Nuclear Fusion **39** (1999) 1489.

- [18] MATSUNAGA, G., AIBA, N., SHINOHARA, K., et al., Phys. Rev. Lett. **103** (2009) 045001.
- [19] OKABAYASHI, M., BOGATU, I., CHANCE, M., et al., Nuclear Fusion **49** (2009) 125003.
- [20] MATSUNAGA, G., SHINOHARA, K., AIBA, N., et al., Nuclear Fusion **50** (2010) 084003.
- [21] MATSUNAGA, G., AIBA, N., SHINOHARA, K., et al., Nuclear Fusion **53** (2013) 073046.
- [22] MATSUNAGA, G., OKABAYASHI, M., AIBA, N., et al., Nuclear Fusion **53** (2013) 123022.
- [23] OKABAYASHI, M., MATSUNAGA, G., DEGRASSIE, J. S., et al., Physics of Plasmas **18** (2011) 056112.
- [24] HEIDBRINK, W. W., AUSTIN, M. E., FISHER, R. K., et al., Plasma Physics and Controlled Fusion **53** (2011) 085028.
- [25] HAO, G. Z., WANG, A. K., LIU, Y. Q., and QIU, X. M., Phys. Rev. Lett. **107** (2011) 015001.
- [26] TODO, Y. and SATO, T., Physics of Plasmas **5** (1998) 1321.
- [27] TODO, Y., Physics of Plasmas **13** (2006) 082503.
- [28] TODO, Y., BERK, H., and BREIZMAN, B., Nuclear Fusion **50** (2010) 084016.
- [29] PEI, Y., XIANG, N., HU, Y., et al., Physics of Plasmas **24** (2017) 032507.
- [30] WANG, J., TODO, Y., WANG, H., and WANG, Z., Nuclear Fusion **60** (2020) 112012.
- [31] TODO, Y., SATO, M., WANG, H., IDOUAKASS, M., and SEKI, R., Plasma Physics and Controlled Fusion **63** (2021) 075018.
- [32] CHEN, L., Physics of Plasmas **1** (1994) 1519.
- [33] ZHANG, W., HOLOD, I., LIN, Z., and XIAO, Y., Physics of Plasmas **19** (2012) 022507.
- [34] MA, R., ZONCA, F., and CHEN, L., Physics of Plasmas **22** (2015) 092501.
- [35] TOBIAS, B. J., CLASSEN, I. G. J., DOMIER, C. W., et al., Phys. Rev. Lett. **106** (2011) 075003.
- [36] HU, Y., TODO, Y., PEI, Y., et al., Physics of Plasmas **23** (2016) 022505.
- [37] FU, G. Y., PARK, W., STRAUSS, H. R., et al., Physics of Plasmas **13** (2006) 052517.
- [38] HEIDBRINK, W. W., STRAIT, E. J., CHU, M. S., and TURNBULL, A. D., Phys. Rev. Lett. **71** (1993) 855.
- [39] PORCELLI, F., Plasma Physics and Controlled Fusion **33** (1991) 1601.
- [40] WHITE, R. B., RUTHERFORD, P. H., COLESTOCK, P., and BUSSAC, M. N., Phys. Rev. Lett. **60** (1988) 2038.
- [41] HU, B., BETTI, R., and MANICKAM, J., Physics of Plasmas **13** (2006) 112505.
- [42] BERK, H., BREIZMAN, B., and PEKKER, M., Nuclear Fusion **35** (1995) 1713.
- [43] WANG, H., TODO, Y., and KIM, C. C., Phys. Rev. Lett. **110** (2013) 155006.
- [44] BROCHARD, G., DUMONT, R., LÜTJENS, H., et al., Nuclear Fusion **60** (2020) 126019.
- [45] HSU, C. T. and SIGMAR, D. J., Physics of Fluids B: Plasma Physics **4** (1992) 1492.